

# Volumetric spherical polynomials

Cite as: AIP Advances **9**, 065107 (2019); <https://doi.org/10.1063/1.5086695>

Submitted: 21 December 2018 . Accepted: 03 June 2019 . Published Online: 12 June 2019

L. Kerby 



[View Online](#)



[Export Citation](#)



[CrossMark](#)

AVS Quantum Science

Co-published with AIP Publishing



Coming Soon!

# Volumetric spherical polynomials

Cite as: AIP Advances 9, 065107 (2019); doi: 10.1063/1.5086695

Submitted: 21 December 2018 • Accepted: 3 June 2019 •

Published Online: 12 June 2019



View Online



Export Citation



CrossMark

L. Kerby<sup>a)</sup>

## AFFILIATIONS

Computer Science and Informatics, Idaho State University, Pocatello, Idaho 83209, USA and Center for Advanced Energy Studies (CAES), Idaho Falls, Idaho 83401, USA

<sup>a)</sup> Electronic mail: kerblesl@isu.edu

## ABSTRACT

Researchers have found functional-based methods to improve data storage, transfer, and interpretation. These functional expansions have been developed and utilized across a range of geometries, from cartesian to cylindrical to the surfaces of spheres. However, a volumetric spherical basis set had not yet been computationally implemented. This paper presents such a basis set and demonstrates its numerical features and benefits.

© 2019 Author(s). All article content, except where otherwise noted, is licensed under a Creative Commons Attribution (CC BY) license (<http://creativecommons.org/licenses/by/4.0/>). <https://doi.org/10.1063/1.5086695>

## I. INTRODUCTION

Recent years have seen a surge in the use of functional expansions for data storage, transfer, and interpretation.<sup>1–4</sup> Researchers have found functional-based methods to speed computation time, decrease memory requirements, ease multiphysics coupling for both Monte Carlo and deterministic modeling codes, and/or aid in detection of important data features. Common basis sets implemented thus far include Legendre polynomials for cartesian-based two- or three-dimensional geometries, Zernike polynomials for circular geometries, Zernike-Legendre combined polynomials for cylindrical geometries, and spherical harmonics for spherical surface geometries. This paper outlines volumetric spherical functional expansions, which would be useful to advance research across applications involving solid spheres (i.e. advanced nuclear reactors utilizing spherical TRISO fuel pellets where modeling of temperature, for example, on both the surface and inside the sphere is relevant).

## II. SPHERICAL POLYNOMIALS

Spherical polynomials are a combination of the standing waves on the surface of a sphere (spherical harmonics,  $Y_l^m(\theta, \varphi)$ ) and a radial function, as shown in Eq. 1:

$$K_l^m(\rho, \theta, \varphi) = R_l^{|m|}(\rho) Y_l^m(\theta, \varphi), \quad (1)$$

where  $(l - m)$  is even with  $l \geq |m| \geq 0$ ,  $\rho$  is the radial distance,  $\theta$  is the polar angle, and  $\varphi$  is the azimuthal angle. These polynomials

are a dimensional expansion of the two-dimensional Zernike polynomials, which have a radial component multiplied by the standing waves on a circle (i.e., sines and cosines). The radial functions of both the Zernike polynomials and these volumetric polynomials are special Jacobi polynomials, with  $\alpha = 0$  and  $\beta = 2$  in the case of volumetric spherical polynomials (and a linear transformation to map to the  $[0,1]$  interval). Jacobi polynomials have been utilized numerically to solve differential equations.<sup>5</sup> Previous research has examined the efficiency of other special Jacobi polynomials (Zernike and Legendre polynomials) as a multiphysics coupling technique and as a replacement for meshed solution fields, and found the use of these polynomials promising.<sup>6–8</sup> Furthermore, the computational efficiency of using Chebyshev polynomials to solve linear quadratic optimal control was studied by Driscoll and Dziedzki.<sup>9</sup>

The volumetric spherical polynomials shown in this paper are orthonormal and are limited to the range of  $-1$  to  $1$ , i.e.  $|K_l^m(\rho, \theta, \varphi)| \leq 1$ . Either the general complex spherical harmonics or the real spherical harmonics may be utilized, depending on the simulation space of the user. The radial function is defined in Eq. 2:

$$R_l^{|m|}(\rho) = N_l \sum_{n=0}^{\frac{l-|m|}{2}} (-1)^n \binom{l-n+\frac{1}{2}}{n} \binom{\frac{l}{2}-2n+\frac{1}{2}}{\frac{l-|m|}{2}-n} \rho^{l-2n}, \quad (2)$$

where the normalization factor  $N_l$  is

$$N_l = \sqrt{2l+3}. \quad (3)$$

The radial functions  $R_l^{|m|}(\rho)$  are defined on  $0 \leq \rho \leq 1$  for even  $(l - |m|) \geq 0$  (else  $R_l^{|m|}(\rho)$  is zero). The use of binomial coefficient tables is recommended to reduce computation time; recall that  $(\frac{1}{2})! = \frac{1}{2}\Gamma(\frac{1}{2}) = \frac{\sqrt{\pi}}{2}$ . The first several radial polynomials, up to  $l = 4$ , are listed in Table I.

The radial functions have the following orthogonality:

$$\int_0^1 \rho^2 R_l^{|m|}(\rho) R_{l'}^{|m'|}(\rho) d\rho = \delta_{l,l'} \delta_{m,m'}. \quad (4)$$

The Laplace form of spherical harmonics, with or without the Condon-Shortley phase, have the following orthonormality:

$$\int_{\theta=0}^{\pi} \int_{\varphi=0}^{2\pi} Y_l^m(\theta, \varphi) Y_{l'}^{m'}(\theta, \varphi) d\Omega = \delta_{l,l'} \delta_{m,m'}, \quad (5)$$

where in spherical coordinates  $d\Omega = \sin \theta d\theta d\varphi$ . Therefore, the volumetric spherical polynomials  $K_l^m(\rho, \theta, \varphi)$  presented in this paper are orthonormal according to Eq. 6:

$$\int K_l^m(\rho, \theta, \varphi) K_{l'}^{m'}(\rho, \theta, \varphi) d^3r = \delta_{l,l'} \delta_{m,m'}, \quad (6)$$

where in spherical coordinates  $d^3r = \rho^2 \sin \theta d\rho d\theta d\varphi$ .

## A. Transform

Functional Expansions (FEs) are a promising and mathematically-sound tool for representing distributions where meshes or tallies might otherwise be used. A sufficiently smooth solution field over a unit sphere  $F(\rho, \theta, \varphi)$  can be represented in terms of its spherical polynomial coefficients  $c_l^m$ :

$$F(\rho, \theta, \varphi) = \sum_{m,l} c_l^m K_l^m(\rho, \theta, \varphi). \quad (7)$$

This is similar to how periodic functions have an orthogonal representation with the Fourier series.  $F(\rho, \theta, \varphi)$  can be a function or a meshed or tallied distribution. An infinite-series FE, i.e. as  $l \rightarrow \infty$ , will theoretically reproduce the original distribution perfectly. Due to computational constraints, in practice the series is truncated at a sufficiently large order  $l$ . The coefficients  $c_l^m$  are defined as

$$c_l^m = \int F(\rho, \theta, \varphi) K_l^m(\rho, \theta, \varphi) d^3r. \quad (8)$$

In Monte Carlo algorithms, for the purpose of tallying a score  $E$  with weight  $w$  at position  $(\rho, \theta, \varphi)$  using Functional Expansion

TABLE I. The first several radial polynomials  $R_l^{|m|}(\rho)$ , up thru  $l = 4$ .

$R_0^0(\rho)$	$\sqrt{3}$
$R_1^1(\rho)$	$\sqrt{5}\rho$
$R_2^0(\rho)$	$\sqrt{7}(2.5\rho^2 - 1.5)$
$R_2^2(\rho)$	$\sqrt{7}\rho^2$
$R_3^3(\rho)$	$3(3.5\rho^3 - 2.5\rho)$
$R_3^3(\rho)$	$3\rho^3$
$R_4^0(\rho)$	$\sqrt{11}(7.875\rho^4 - 8.75\rho^2 + 1.875)$
$R_4^2(\rho)$	$\sqrt{11}(4.5\rho^4 - 3.5\rho^2)$
$R_4^4(\rho)$	$\sqrt{11}\rho^4$

Tallies (FETs), the tally for coefficient  $c_l^m$  can be incremented by a value

$$K_l^m(\rho, \theta, \varphi) E w \quad (9)$$

taking care to also increase the total weight  $W$  by an amount  $w$ .

While FEs and FETs have noted advantages in data storage, transfer, and interpretation, several limitations should be noted. They display Gibbs phenomenon near discontinuities, and therefore piecewise-continuous FEs/FETs should be used over significant discontinuities in the solution field. They are also limited somewhat to the native geometry of each FE/FET, i.e. using Zernike polynomials requires a unit circle and using these spherical polynomials requires a unit sphere. The user must transform their simulation space to the required FE space and/or use the appropriate FE for their geometry.

## B. Graphical representation

For this section real Laplace spherical harmonics (i.e. tesseral spherical harmonics) will be utilized. These are represented as:

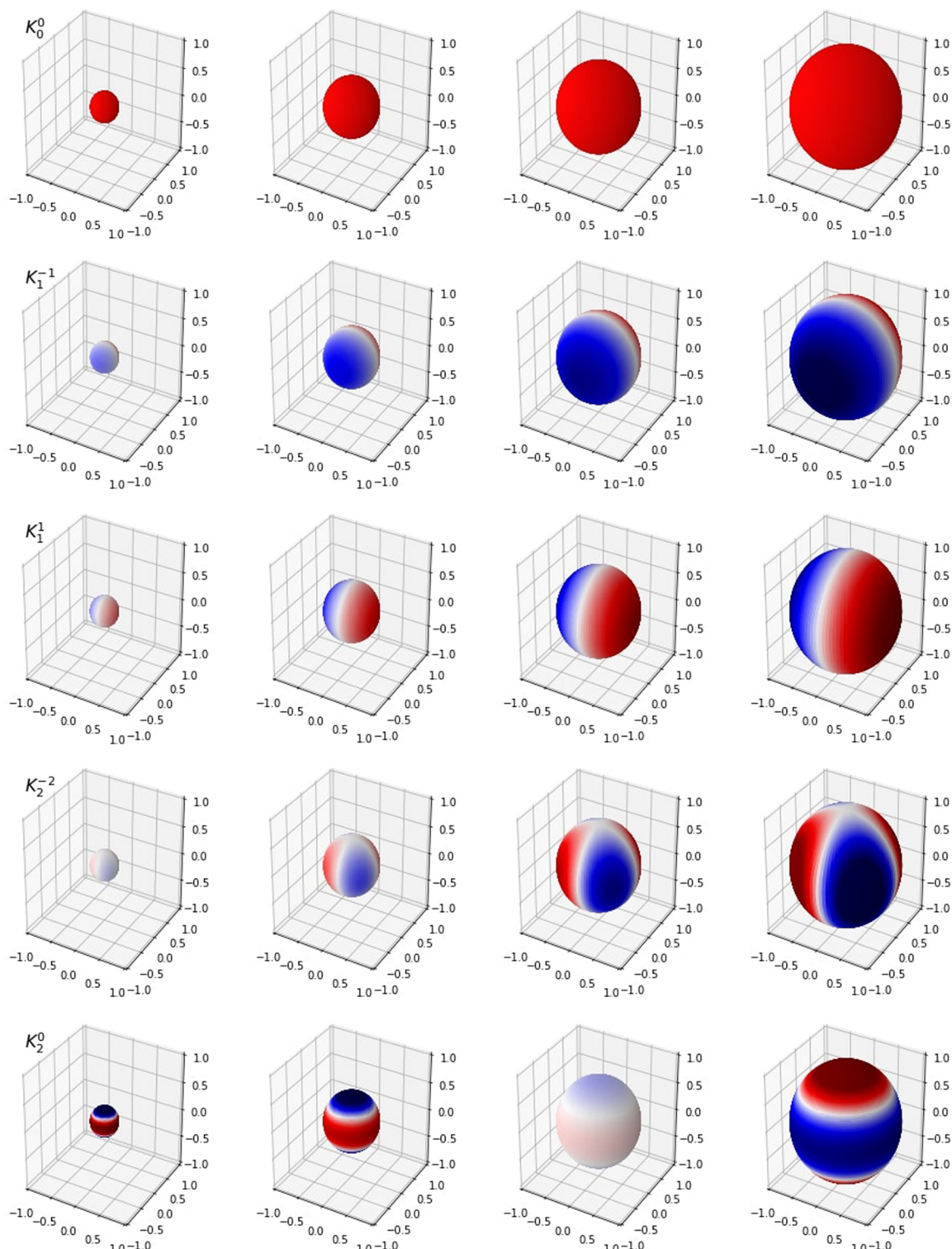
$$Y_l^m(\theta, \varphi) = \begin{cases} \sqrt{2N_l^{|m|}} P_l^{|m|}(\cos\theta) \sin(|m|\varphi) & m < 0 \\ N_l^{|m|} P_l^m(\cos\theta) & m = 0 \\ \sqrt{2N_l^{|m|}} P_l^m(\cos\theta) \cos(m\varphi) & m > 0 \end{cases} \quad (10)$$

where the normalization factor  $N_l^{|m|}$  is

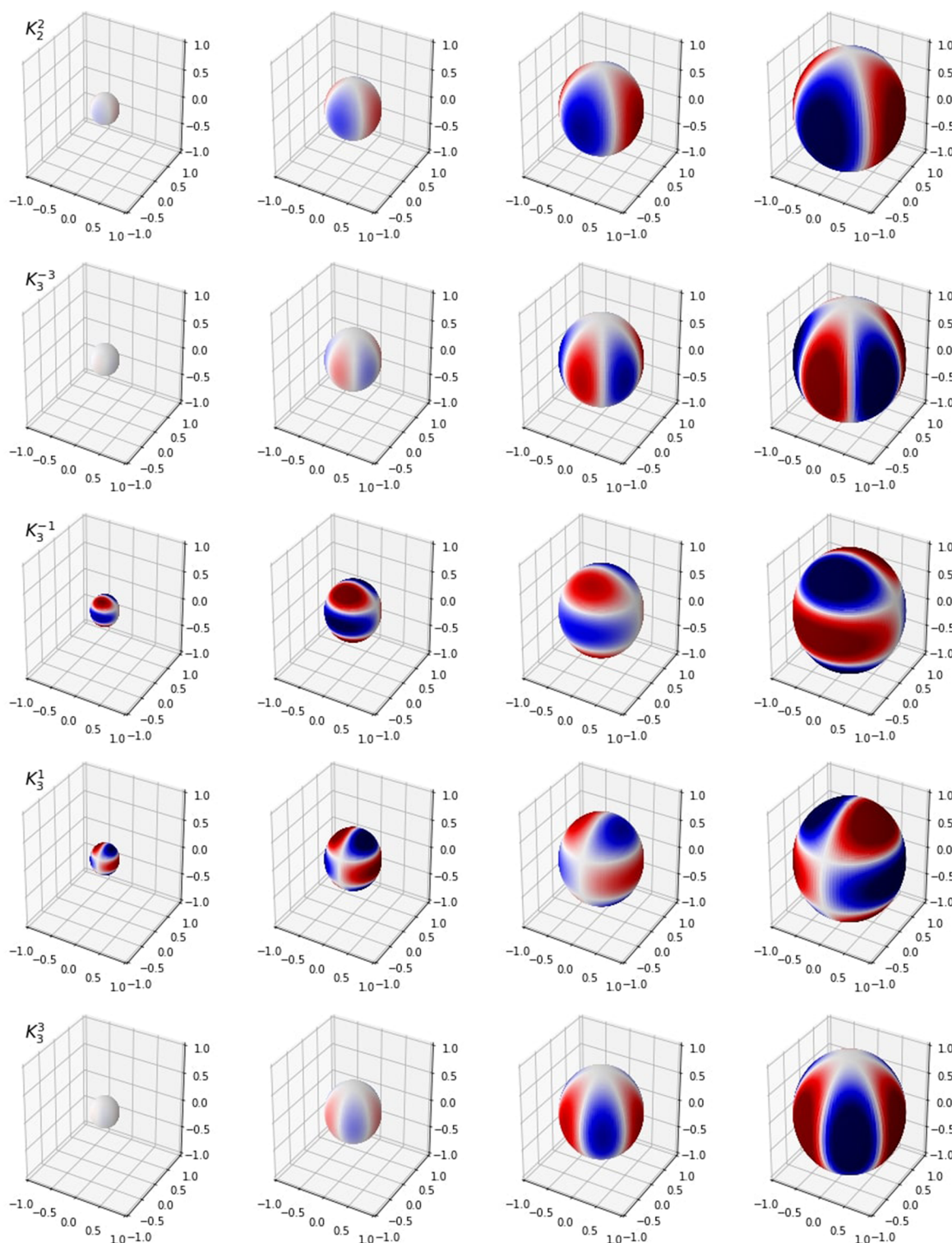
$$N_l^{|m|} = \sqrt{\frac{(2l+1)}{4\pi} \frac{(l-|m|)!}{(l+|m|)!}} \quad (11)$$

TABLE II. The first several real Laplace spherical harmonics  $Y_l^m(\theta, \varphi)$  with  $(l - m)$  even, up thru  $l = 4$ .

$Y_0^0(\theta, \varphi)$	$\sqrt{\frac{1}{4\pi}}$
$Y_1^{-1}(\theta, \varphi)$	$\sqrt{\frac{3}{4\pi}} \sin\theta \sin\varphi$
$Y_1^1(\theta, \varphi)$	$\sqrt{\frac{3}{4\pi}} \sin\theta \cos\varphi$
$Y_2^{-2}(\theta, \varphi)$	$\sqrt{\frac{15}{16\pi}} \sin^2\theta \sin(2\varphi)$
$Y_2^0(\theta, \varphi)$	$\sqrt{\frac{5}{16\pi}} (3\cos^2\theta - 1)$
$Y_2^2(\theta, \varphi)$	$\sqrt{\frac{15}{16\pi}} \sin^2\theta \cos(2\varphi)$
$Y_3^{-3}(\theta, \varphi)$	$\sqrt{\frac{35}{32\pi}} \sin^3\theta \sin\varphi (3 - 4\sin^2\varphi)$
$Y_3^{-1}(\theta, \varphi)$	$\sqrt{\frac{21}{32\pi}} \sin\theta \sin\varphi (5\cos^2\theta - 1)$
$Y_3^1(\theta, \varphi)$	$\sqrt{\frac{21}{32\pi}} \sin\theta \cos\varphi (5\cos^2\theta - 1)$
$Y_3^3(\theta, \varphi)$	$\sqrt{\frac{35}{32\pi}} \sin^3\theta \cos\varphi (4\cos^2\varphi - 3)$
$Y_4^{-4}(\theta, \varphi)$	$\sqrt{\frac{315}{64\pi}} \sin^4\theta \sin(2\varphi) (1 - 2\sin^2\varphi)$
$Y_4^{-2}(\theta, \varphi)$	$\sqrt{\frac{45}{64\pi}} \sin^2\theta \sin(2\varphi) (7\cos^2\theta - 1)$
$Y_4^0(\theta, \varphi)$	$\sqrt{\frac{9}{256\pi}} (35\cos^4\theta - 30\cos^2\theta + 3)$
$Y_4^2(\theta, \varphi)$	$\sqrt{\frac{45}{64\pi}} \sin^2\theta (2\cos^2\varphi - 1) (7\cos^2\theta - 1)$
$Y_4^4(\theta, \varphi)$	$\sqrt{\frac{315}{256\pi}} \sin^4\theta (8\cos^4\varphi - 8\cos^2\varphi + 1)$



**FIG. 1.** Spherical shells of  $K_l^m(\rho, \theta, \phi)$  shown at  $\rho = 0.25, 0.5, 0.75$ , and  $1$  (from left to right) for volumetric spherical polynomials  $K_0^0, K_1^{-1}, K_1^1, K_2^{-2}$ , and  $K_2^0$ . Dark red values indicate  $K_l^m$  approaches  $+1$  and dark blue values indicate  $K_l^m$  approaches  $-1$ ; however note that the coefficients for each  $K_l^m$  mode can be negative, effectively switching positive and negative values.



**FIG. 2.** Spherical shells of  $K_l^m(\rho, \theta, \varphi)$  shown at  $\rho = 0.25, 0.5, 0.75$ , and  $1$  (from left to right) for volumetric spherical polynomials  $K_2^2, K_3^{-3}, K_3^{-1}, K_3^1$ , and  $K_3^3$ . Dark red values indicate  $K_l^m$  approaches  $+1$  and dark blue values indicate  $K_l^m$  approaches  $-1$ ; however note that the coefficients for each  $K_l^m$  mode can be negative, effectively switching positive and negative values.

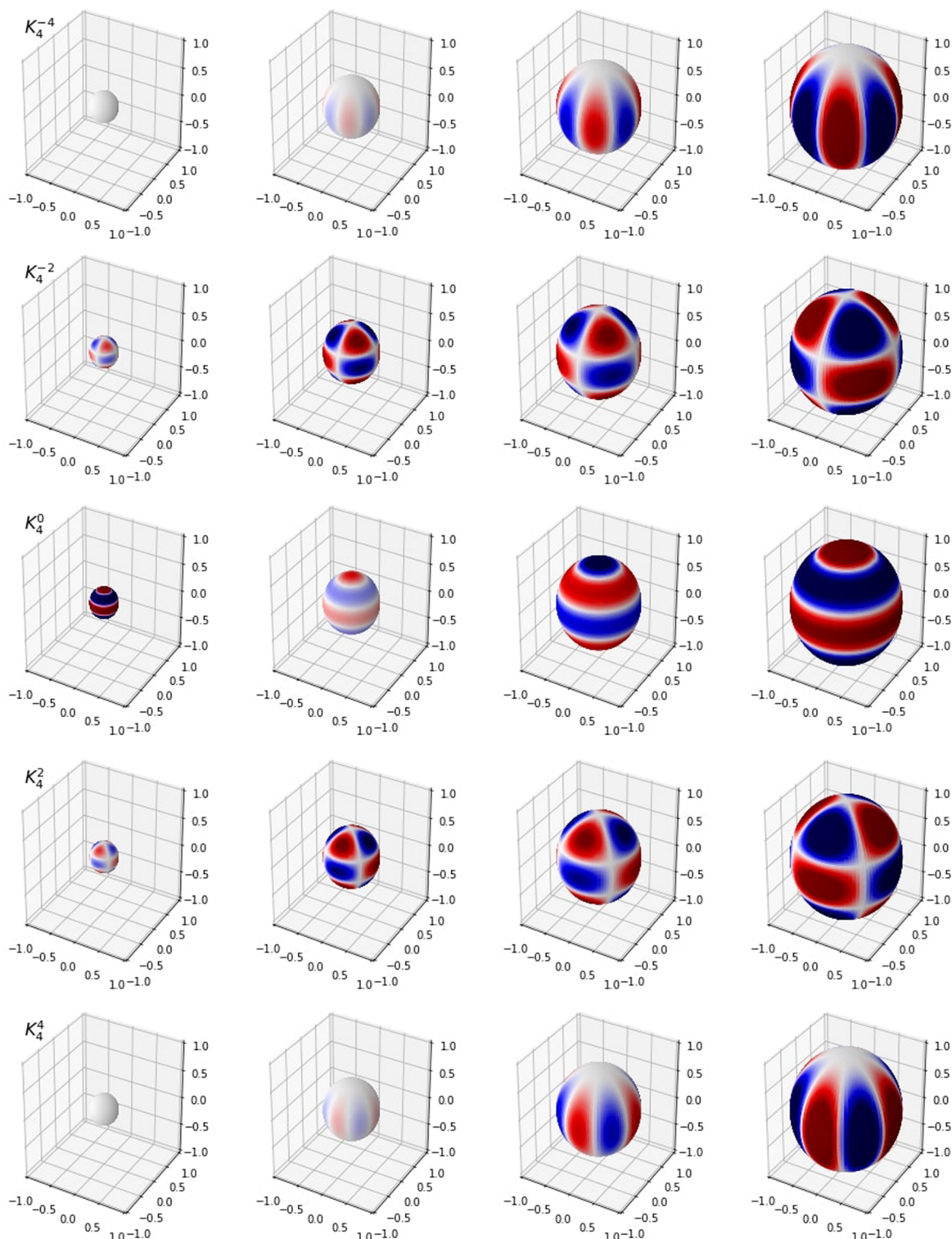


**FIG. 3.** Spherical shells of  $K_l^m(\rho, \theta, \varphi)$  shown at  $\rho = 0.25, 0.5, 0.75, \text{ and } 1$  (from left to right) for volumetric spherical polynomials  $K_4^{-4}, K_4^{-2}, K_4^0, K_4^2$ , and  $K_4^4$ . Dark red values indicate  $K_l^m$  approaches +1 and dark blue values indicate  $K_l^m$  approaches -1; however note that the coefficients for each  $K_l^m$  mode can be negative, effectively switching positive and negative values.

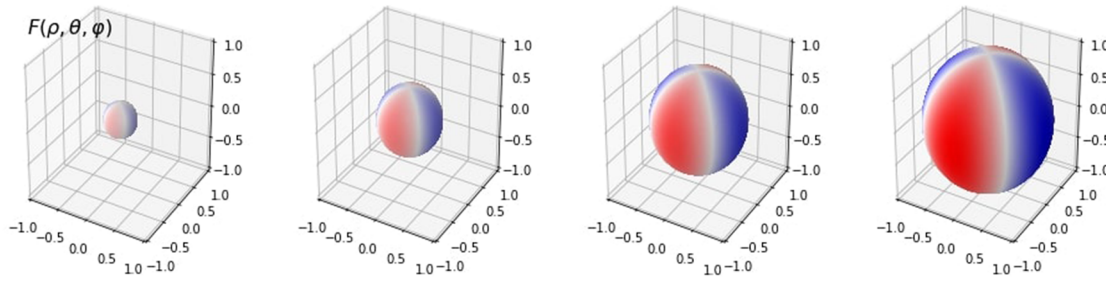


**FIG. 4.** Spherical shells of  $F(\rho, \theta, \varphi) = \rho \sin \theta \cos (\varphi - \pi/4) \sin (\varphi - \pi/4)$  shown at  $\rho = 0.25, 0.5, 0.75$ , and  $1$  (from left to right). Dark red values indicate  $F(\rho, \theta, \varphi)$  is positive and dark blue values indicate  $F(\rho, \theta, \varphi)$  is negative.

and the associated Legendre polynomials are

$$P_l^m(\cos\theta) = \sin^m\theta \frac{d^m}{d(\cos\theta)^m} P_l(\cos\theta) \quad (12)$$

for positive  $m$ , and

$$P_l^{-m}(\cos\theta) = \frac{(l-m)!}{(l+m)} P_l^m(\cos\theta) \quad (13)$$

for negative  $m$ . The first several  $(l - m)$ -even real spherical harmonics, up to  $l = 4$ , are shown in Table II. They do not contain the Condon-Shortley phase factor  $(-1)^m$ , commonly added in quantum mechanical applications. The complex spherical harmonics may be used in the volumetric spherical polynomials  $K_l^m(\rho, \theta, \varphi)$  if the domain space includes the imaginary plane, however for graphical purposes the real form is chosen here.

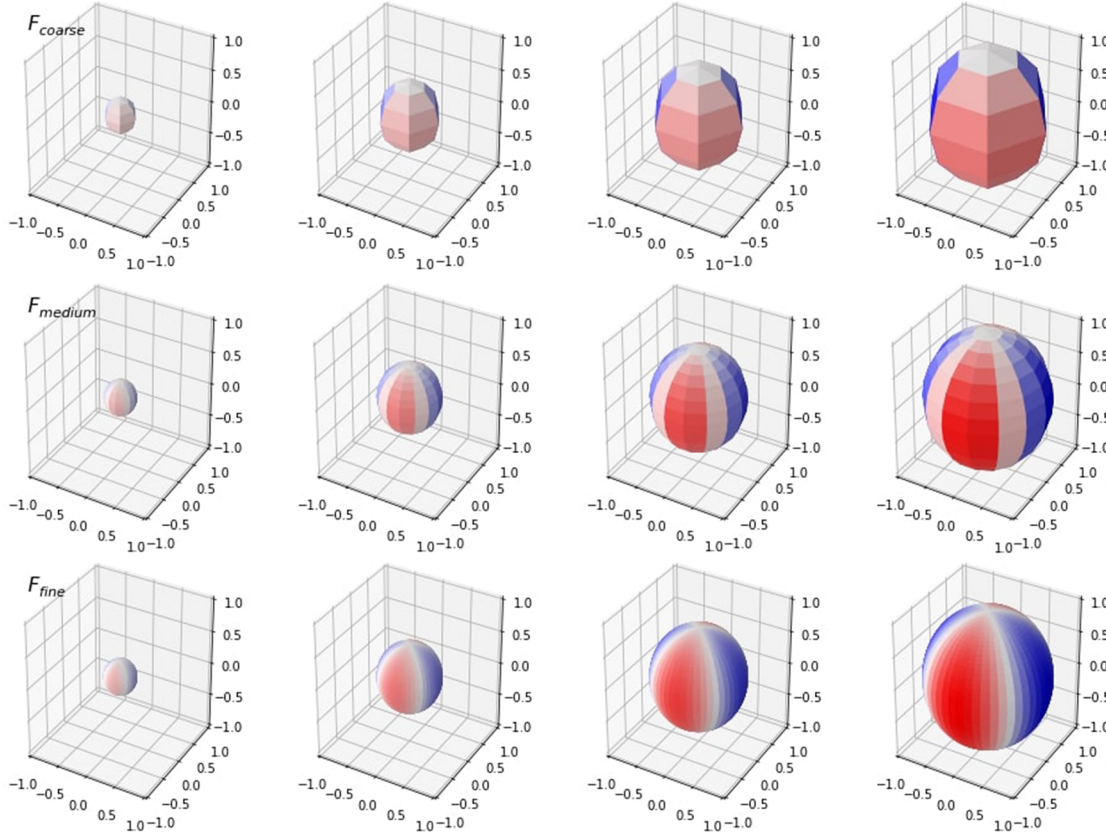


**FIG. 5.** Spherical shells of  $F(\rho, \theta, \varphi) = \rho \sin \theta \cos (\varphi - \pi/4) \sin (\varphi - \pi/4)$  shown at  $\rho = 0.25, 0.5, 0.75$ , and  $1$  (from left to right) for three different mesh sizes:  $7 \times 7 \times 7$  coarse (top),  $15 \times 15 \times 15$  medium (middle), and  $50 \times 50 \times 50$  fine (bottom). Dark red values indicate  $F(\rho, \theta, \varphi)$  is positive and dark blue values indicate  $F(\rho, \theta, \varphi)$  is negative.

Graphical representations of the first 15 modes of  $K_l^m(\rho, \theta, \varphi)$ , up thru  $l = 4$ , are shown in Figs. 1–3.

### C. Example

As an example, spherical polynomials will be used to describe the function

$$F(\rho, \theta, \varphi) = \rho \sin \theta \cos(\varphi - \pi/4) \sin(\varphi - \pi/4), \quad (14)$$

which is plotted in Fig. 4.

Three different mesh sizes will be compared with FEs: coarse ( $7 \times 7 \times 7$ ), medium ( $15 \times 15 \times 15$ ), and fine ( $50 \times 50 \times 50$ ). Graphs of  $F(\rho, \theta, \varphi)$  for these three meshes are shown in Fig. 5.

The FE transform of each of these three meshes using  $K_l^m(\rho, \theta, \varphi)$ , up through order  $l = 4$ , is shown in Fig. 6. Note that the FE transforms are continuous, regardless of the mesh size of the underlying distribution. For this case, the FE transform of the medium mesh is nearly identical to the FE transform of the fine mesh, i.e. little is gained by the extra resolution of the fine mesh. The accuracy of the FE transform in general depends upon the mesh size of the distribution being transformed as well as the number of orders  $l$  used in  $K_l^m(\rho, \theta, \varphi)$ .

The storage sizes of the  $F(\rho, \theta, \varphi)$  solution field for the three mesh sizes and the spherical polynomial FE is shown in Table III.

The FE file size is smaller than the coarse mesh file size, and nearly one thousand times smaller than the fine mesh file size. Note that regardless of the original distribution's mesh size, the resulting FE storage size is only dependent upon the order  $l$  used in the transform.

Upon inspection of the coefficient table (Table IV) it is apparent the  $K_2^2$  mode is dominant with secondary contributions by  $K_4^2$ ,  $K_4^4$ ,  $K_1^1$ , and other modes, in decreasing order. For more complex solution fields higher orders of  $l$  would likely be required for accuracy as well as cross-term coefficients, as discussed in Section II D.

This example shows how to transform a solution field after it is fully formed (i.e. as is done in deterministic codes). While this may seem to add to computation time, studies have shown that once a mesh reaches a medium size it is actually more efficient to transform to an FE to store and transfer as opposed to storing and transferring a large dataset.<sup>10</sup> The computation time increase is offset by gains in memory latency. However, in Monte Carlo codes, the functional expansions are not done as an extra step at the end, but rather replace the conventional mesh tallying methods in the solution computation itself. Traditionally, each event is scored to a bin or mesh (be it spatial or energy or time etc). In applying Functional Expansion Tallies (FETs), each event is scored instead to the coefficients

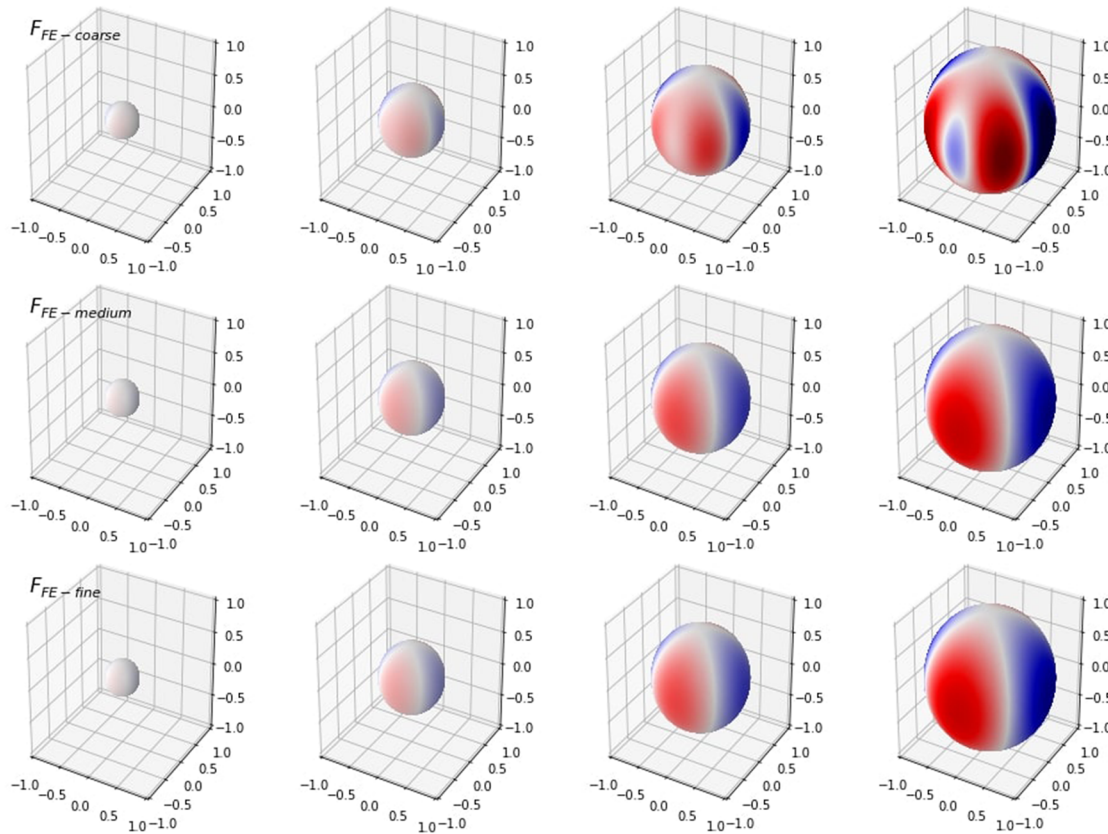


**FIG. 6.** Spherical shells of the  $K_l^m$  functional expansion transform of  $F(\rho, \theta, \varphi)$  for the coarse (top), medium (middle), and fine (bottom) meshes, shown at  $\rho = 0.25, 0.5, 0.75$ , and 1 (from left to right). Dark red values indicate the FE transform is positive and dark blue values indicate it is negative.

**TABLE III.** Table of mesh or FE file storage size.

Type	Storage Size (KB)
Coarse Mesh	2.8
Medium Mesh	26.4
Fine Mesh	976
FE	1.0

of the functional expansion. This means there is no redundancy of computation—the solution field is tallied directly to the FE space rather than the mesh space and then transformed. For this reason FETs are particularly promising. These techniques have previously been applied across a variety of different spatial geometries, but the methods would easily carry over to using FETs to tally across energy and time dimensions as well. For more information on FETs, see Refs. 1, 3, 7, 8, and 10.

#### D. Fully convolved $K_{l,l'}^{m,m'}(\rho, \theta, \varphi)$

The  $K_l^m(\rho, \theta, \varphi)$  developed thus far are separable between  $(\rho)$  and  $(\theta, \varphi)$  and the coefficient matrix has been diagonalized. However, it is not difficult to develop a fully convolved basis set,

$$K_{l,l'}^{m,m'}(\rho, \theta, \varphi) = R_l^{|m|}(\rho) Y_{l'}^{m'}(\theta, \varphi), \quad (15)$$

containing coefficient cross terms. The coefficient matrix for  $K_{l,l'}^{m,m'}(\rho, \theta, \varphi)$  is displayed in Eq. 16. The diagonalized form  $K_l^m(\rho, \theta, \varphi)$  is constrained by  $m = m'$  and  $l = l'$  and only consists of the diagonal terms (bolded).

**TABLE IV.** Table of  $c_l^m$  spherical polynomial coefficients calculated from the  $F(\rho, \theta, \varphi)$  fine mesh with  $l = 4$ .

Coefficient	Value
$c_0^0$	$6.706e-5$
$c_1^{-1}$	$-1.449e-17$
$c_1^1$	$1.265e-4$
$c_2^{-2}$	$6.358e-17$
$c_2^0$	$-4.772e-6$
$c_2^2$	$-0.4456$
$c_3^{-3}$	$4.590e-17$
$c_3^{-1}$	$-4.891e-19$
$c_3^1$	$1.879e-13$
$c_3^3$	$2.980e-4$
$c_4^{-4}$	$6.420e-17$
$c_4^{-2}$	$-1.885e-18$
$c_4^0$	$1.238e-7$
$c_4^2$	$0.01006$
$c_4^4$	$4.279e-4$

$$\begin{bmatrix} c_{0,0}^{0,0} & c_{0,1}^{0,-1} & c_{0,1}^{0,1} & c_{0,2}^{0,-2} & c_{0,2}^{0,0} & c_{0,2}^{0,2} & \dots \\ c_{1,0}^{-1,0} & \mathbf{c}_{1,1}^{-1,-1} & c_{1,1}^{-1,1} & c_{1,2}^{-1,-2} & c_{1,2}^{-1,0} & c_{1,2}^{-1,2} & \dots \\ c_{1,0}^{1,0} & c_{1,1}^{1,-1} & \mathbf{c}_{1,1}^{1,1} & c_{1,2}^{1,-2} & c_{1,2}^{1,0} & c_{1,2}^{1,2} & \dots \\ c_{2,0}^{-2,0} & c_{2,1}^{-2,-1} & c_{2,1}^{-2,1} & \mathbf{c}_{2,2}^{-2,-2} & c_{2,2}^{-2,0} & c_{2,2}^{-2,2} & \dots \\ c_{2,0}^{0,0} & c_{2,1}^{0,-1} & c_{2,1}^{0,1} & c_{2,2}^{0,-2} & \mathbf{c}_{2,2}^{0,0} & c_{2,2}^{0,2} & \dots \\ c_{2,0}^{2,0} & c_{2,1}^{2,-1} & c_{2,1}^{2,1} & c_{2,2}^{2,-2} & c_{2,2}^{2,0} & \mathbf{c}_{2,2}^{2,2} & \dots \\ \vdots & \vdots & \vdots & \vdots & \vdots & \vdots & \ddots \end{bmatrix} \quad (16)$$

Using a diagonalized FE assumes the coefficient cross-terms are zero or near zero. When this assumption is not valid, fully convolved FEs should be used. The storage size of a fully convolved FE will be significantly larger than that for similar-ordered diagonalized FEs.

The weakness of diagonalized FEs can be seen in the example. Notice that the FE goes to zero faster as  $\rho \rightarrow 0$  than the actual  $F(\rho, \theta, \varphi)$  (this can be observed from looking at the  $\rho = 0.25$  and  $0.5$  shells in the figures and noting that the FE figure is whiter). This occurs because the dominant mode,  $K_2^2$ , has a  $\rho^2$  factor, while the  $F(\rho, \theta, \varphi)$  dependency is just  $\rho$ . Without coefficient cross terms, there is no way to model both the  $\sin\varphi\cos\theta$  and  $\rho$  dependencies.

The Zernike polynomials share similar separability and diagonalization features as the spherical polynomials  $K_l^m(\rho, \theta, \varphi)$ . They may also be expanded to include coefficient cross-terms in a similar manner as shown here. Lastly, this coefficient-cross-terms decision is encountered in implementing multi-dimensional Legendre polynomials as well, albeit in a slightly different way as in that case the simplification is to keep the first row and first column only and discard the remainder of the coefficient matrix. Utilizing sparse matrix methods may provide a useful compromise between diagonalized coefficients and the full coefficient matrix.

### III. CONCLUSIONS

Volumetric spherical polynomials are a valuable part of the functional expansion toolbox.  $K_l^m(\rho, \theta, \varphi)$  are orthonormal and have the property that  $K_l^m(\rho, \theta, \varphi) \leq 1$ . Memory requirements for  $K_l^m(\rho, \theta, \varphi)$  polynomials are significantly less than meshed distributions, and are not dependent on the size of the mesh transformed from but only on the order  $l$  used in the transformation. Furthermore, functional expansions are continuous and inspection of dominant modes can lead to feature extraction of the data. For transformation of complicated solution fields, use of the fully convolved  $K_{l,-l}^{m,-m}(\rho, \theta, \varphi)$  is recommended.

When using  $K_l^m(\rho, \theta, \varphi)$  in deterministic codes, an extra computational step is necessary to transform the meshed solution field to the functional expansion space. Previous studies have found this computation time can be offset by the advantages of memory and latency reduction, depending upon mesh size.<sup>10</sup> Using functional expansion-based methods in Monte Carlo codes—FETs—is particularly promising in part because there is no such redundancy

of computation: solutions are tallied directly to the  $c_l^m$  coefficients instead of the meshed geometry. FETs have shown increased accuracy, improved convergence and Figure of Merit (FOM) properties, decreased storage and memory requirements, and easier coupling of disparate codes.

## ACKNOWLEDGMENTS

This research was supported by the Exascale Computing Project (17-SC-20-SC), a collaborative effort of two U.S. Department of Energy organizations (Office of Science and the National Nuclear Security Administration) responsible for the planning and preparation of a capable exascale ecosystem, including software, applications, hardware, advanced system engineering, and early testbed platforms, in support of the nation's exascale computing imperative.

## REFERENCES

- <sup>1</sup>B. Wendt, L. Kerby, A. Tumulak, and J. Leppänen, "Advancement of functional expansion capabilities: Implementation and optimization in Serpent 2," *Nuclear Engineering and Design* **334**, 138 (2018).
- <sup>2</sup>B. Wendt, A. Novak, L. Kerby, and P. Romano, "Integration of functional expansion methodologies as a MOOSE module," in *Proc. Physics of Reactors Conference (PHYSOR)* (Cancun, Mexico, 2018).
- <sup>3</sup>M. Ellis, D. Gaston, B. Forget, and K. Smith, "Preliminary coupling of the Monte Carlo code OpenMC and the multiphysics object-oriented simulation environment for analyzing doppler feedback in Monte Carlo simulations," *Nuclear Science and Engineering* **185**, 184 (2017).
- <sup>4</sup>F. Pfaff, G. Kurz, and U. Hanebeck, "Filtering on the unit sphere using spherical harmonics," in *Proc. IEEE International Conference on Multisensor Fusion and Integration for Intelligent Systems (MFI)* (Daegu, South Korea, 2017).
- <sup>5</sup>B. Guo, J. Shen, and L. Wang, "Generalized Jacobi polynomials functions and their applications," *Applied Numerical Mathematics* **59**, 1011 (2009).
- <sup>6</sup>P. Wilson, T. Evans, and T. Tautges, "Advanced mesh-enabled Monte Carlo capability for multi-physics reactor analysis," in U.S. Department of Energy NEUP Technical Report (2012).
- <sup>7</sup>D. Griesheimer, "Functional expansion tallies for Monte Carlo simulations," Ph.D. thesis, University of Michigan, 2005.
- <sup>8</sup>B. Wendt, Functional expansions methods: Optimizations, characterizations, and multiphysics practices, Ph.D. thesis, Idaho State University, 2018.
- <sup>9</sup>T. Driscoll and J. Dzielski, "Computational efficiency of a functional expansion algorithm for linear quadratic optimal control," in Proc. 31st Conference on Decision and Control, Tucson, AZ, USA, 1992.
- <sup>10</sup>L. Kerby, R. Stewart, B. Grayson, S. Wacker, and B. Wendt, "Year-end report for FY17, Department of Energy, Exascale Computing Project: Coupled Monte Carlo neutronics and fluid flow simulation of small modular reactors; research by Idaho State University," in Technical Report, 2017.